Hybrid QM/MM Molecular Dynamics with AMOEBA Polarizable Embedding

Daniele Loco, Louis Lagardère, Stefano Caprasecca, Filippo Lipparini, Benedetta Mennucci, Jean-Philip Piquemal

Hybrid QM/MM Molecular Dynamics with AMOEBA Polarizable Embedding

Daniele Loco,[†] Louis Lagardère,[‡] Stefano Caprasecca,[†] Filippo Lipparini,[*,¶] Benedetta Mennucci,[*,†] and Jean-Philip Piquemal[*,§,‖,⊥]

[†]*Dipartimento di Chimica e Chimica Industriale, Università di Pisa, via G. Moruzzi 13, I-56124 Pisa, Italy*

[‡]*UPMC Univ. Paris 06, Institut des Sciences du Calcul et des Données, F-75005, Paris, France*

[¶]*Institut für Physikalische Chemie, Universität Mainz, Duesbergweg 10-14, D-55128 Mainz, Germany*

[§]*UPMC Univ. Paris 06, UMR7616, Laboratoire de Chimie Théorique, F-75005, Paris, France*

[‖]*Institut Universitaire de France, Paris Cedex 05, 75231, France*

[⊥]*Department of Biomedical Engineering, The University of Texas at Austin, Austin, Texas 78712, USA*

E-mail: flippari@uni-mainz.de; benedetta.mennucci@unipi.it; jpp@lct.jussieu.fr

Abstract

We present the implementation of a Born-Oppenheimer (BO) hybrid Quantum Mechanics/Molecular Mechanics (QM/MM) Molecular Dynamics (MD) strategy using Density Functional Theory (DFT) and the polarizable AMOEBA force field. This approach couples the Gaussian and Tinker suite of programs through a variational formalism allowing for a full self-consistent relaxation of both the AMOEBA induced dipoles and the DFT electronic density at each MD step. As the DFT SCF cycles are the limiting factor in terms of computational efforts and MD stability, we focus on the latter aspect and compare the Time-Reversible BO (TR–BO) and the Extended BO Lagrangian approaches (XL–BO) to the MD propagation. The XL–BO approach allows for stable, energy-conserving trajectories offering various perspectives for hybrid simulations using polarizable force fields.

1 Introduction

In recent years lots of efforts have been devoted to improve both the efficiency and the applicability of polarizable Molecular Mechanics (MM) force fields. (FF)[1,2] In contrast to standard force fields, polarizable ones include many-body effects, which makes them in principle more flexible and accurate. Naturally, a fully classical description, even if including polarization, is not sufficient for many important chemical and physical problems, such as the study of chemical reactivity and photo-induced processes. In that context, a hybrid QM/MM strategy that couples a polarizable FF with a quantum mechanical (QM) approach represents a very promising strategy as it combines the computational efficiency of an accurate classical model with the required quantum description of the subsystem of interest. Many examples in this direction have been presented so far in the literature, where the polarizable FF can be obtained either in terms of fluctuating charges,[3–6] drude oscillators[7,8] or induced dipoles.[9–17] In the framework of induced dipoles formulations, we recently presented a polarizable QM/MM implementation based on Density Functional Theory (DFT) and the AMOEBA polarizable FF.[18] Such an implementation is based on a variational formalism[19,20] and couples the induced dipoles and the electronic density in a fully self-consistent way. Both ground and excited-state energies have been presented; the latter are obtained within the framework of time-dependent DFT (TD-DFT), either in a linear response or in a state-specific picture. Our work complements several other QM/AMOEBA implementations within various other suite of programs, such as LICHEM,[21] ONETEP/TINKER[22] and the Q-Chem/LibEFP interface.[23]

In our last work, however, the QM/AMOEBA computations were performed on snapshots obtained with a purely classical MD simulation. In other words, the MD and the QM/MM calculations where decoupled and performed using different methods. We pursue here a genuine QM/MM MD strategy, which is achieved by coupling together the Tinker[24] MD package and the Gaussian[25] suite of programs and by implementing analytical gradients for the polarizable QM/AMOEBA energy.

QM/MM MD simulations[26–29] have been proposed both within a Born-Oppenheimer MD (BOMD)[30] and Lagrangian Car-Parrinello MD (CPMD).[31] In BOMD the electronic QM(/MM) equations are solved at each time-step to obtain the ground state potential energy and forces acting on the nuclei. In CPMD the electronic degrees of freedom are rather propagated together with the nuclear ones, which avoids the cost of solving at each step the QM electronic problem. CPMD is thus computationally much more efficient that BOMD. This comes, however, at a cost, as CPMD can produce different results from BOMD.[30,32,33]

The efficiency of BOMD can be majorly improved by improving the initial guess for the SCF equations using information that is available along the trajectory.[32,34–36]

Over the years, many strategies have been proposed to accelerate the SCF procedure in *ab initio* dynamics.[32,34–36] Among them, the time-

reversible BOMD developed by Niklasson and coworkers[37] represents an efficient and accurate method, preserving the time-reversal symmetry, thus avoiding systematic errors in energy, gradients and, consequently, memory effects in the nuclear trajectory and an unphysical systematic drift in the system's total energy.

They observed however that the perfect time-reversibility leads to instabilities under noisy conditions, requiring a sufficiently accurate electronic density for longer simulations. To address this issue, they proposed an Extended Lagrangian approach,[38] including the coupling to a fictitious external "dissipative reservoir" to remove the numerical error fluctuations without introducing any significant energy drift or modification of the nuclear forces.

In the present contribution we apply the Extended Lagrangian formalism in the context of the hybrid QM/AMOEBA BOMD, showing that stable and accurate dynamics can indeed be performed. To do so, we will first recall the working equations for the QM/AMOEBA implementation in a variational formulation. Then a special focus will be given on the presentation of the analytical derivatives of the QM/AMOEBA energy and on the comparison of the two predictor-corrector schemes by Niklasson *et al.*[37,38] that we applied to the computation of the QM part to reduce the computational cost at every hybrid MD step.

2 Polarizable QM/MM with the AMOEBA force field

In this section, we will briefly sum up the coupled QM/AMOEBA equations for an SCF-based QM method. A full derivation can be found in a previous work of some of us.[18] Detailed information on the AMOEBA force field and the way it treats the polarization problem can be found in the relevant literature.[20,39,40]

Here, we report the QM/AMOEBA variational energy functional

$$\begin{aligned}\mathcal{E}(\boldsymbol{P},\boldsymbol{\mu}) &= \mathcal{E}^{\mathrm{QM}}(\boldsymbol{P}) + \mathcal{E}^{\mathrm{MM}}(\boldsymbol{\mu}) + \\ &+\mathcal{E}^{\mathrm{Coup}}(\boldsymbol{P},\boldsymbol{\mu}) = \mathcal{E}^{\mathrm{QM}}(\boldsymbol{P}) + \mathcal{E}^{\mathrm{Env}}(\boldsymbol{P},\boldsymbol{\mu}),\end{aligned} \tag{1}$$

where we introduced an environment term $\mathcal{E}^{\mathrm{Env}}$, which is given by the sum of three contributions:

$$\mathcal{E}^{\mathrm{Env}} = \mathcal{E}^{\mathrm{FF}} + \mathcal{E}^{\mathrm{El}}_{\mathrm{QM/MM}}(\mathbf{P}) + \mathcal{E}^{\mathrm{Pol}}_{\mathrm{QM/MM}}(\boldsymbol{P},\boldsymbol{\mu}). \tag{2}$$

The first term in eq. 2 includes the MM bonded and dispersion-repulsion interactions, which depend on neither the electronic density nor the induced dipoles. This term includes also the "van der Waals" interactions between the classical and quantum subsystems, which in our implementation are treated with the AMOEBA force field. The second term is given by the electrostatic interaction between the AMOEBA static multipoles and the QM density

$$\begin{aligned}\mathcal{E}^{\mathrm{El}}_{\mathrm{QM/MM}}(\boldsymbol{P}) = \boldsymbol{q}^{\dagger}\boldsymbol{V}^{\mathrm{QM}}(\boldsymbol{P}) - \boldsymbol{\mu}_{\mathrm{s}}^{\dagger}\mathbf{E}^{\mathrm{QM}}(\boldsymbol{P}) + \\ -\boldsymbol{\Theta}^{\dagger}\boldsymbol{G}^{\mathrm{QM}}(\boldsymbol{P}),\end{aligned} \tag{3}$$

where q_i, $\vec{\mu}_{\mathrm{s},i}$ and $\boldsymbol{\Theta}_i$ are the fixed charges, dipoles and quadrupoles, respectively, and the potential, field and field gradient produced by the QM density at the i-th MM atom are each written as the sum of a nuclear and an electronic contribution:

$$V^{\mathrm{QM}}(\vec{r}_i;\boldsymbol{P}) = \sum_k^{N_{\mathrm{QM}}} \frac{Z_k}{|\vec{r}_i - \vec{R}_k|} + \sum_{\mu\nu}^{N_{\mathrm{b}}} P_{\mu\nu} V_{\mu\nu}(\vec{r}_i) \tag{4}$$

$$\vec{E}^{\mathrm{QM}}(\vec{r}_i;\boldsymbol{P}) = \sum_k^{N_{\mathrm{QM}}} \frac{Z_k(\vec{r}_i - \vec{R}_k)}{|\vec{r}_i - \vec{R}_k|^3} + \sum_{\mu\nu}^{N_{\mathrm{b}}} P_{\mu\nu} \vec{E}_{\mu\nu}(\vec{r}_i) \tag{5}$$

$$\begin{aligned}[G^{\mathrm{QM}}]^{\alpha\beta}(\vec{r}_i;\boldsymbol{P}) = \sum_k^{N_{\mathrm{QM}}} Z_k \left(\frac{3(r_i^{\alpha} - R_k^{\alpha})(r_i^{\beta} - R_k^{\beta})}{|\vec{r}_i - \vec{R}_k|^5} \right. \\ \left. - \frac{\delta_{\alpha\beta}}{|\vec{r}_i - \vec{R}_k|^3} \right) + \sum_{\mu\nu}^{N_{\mathrm{b}}} P_{\mu\nu} G^{\alpha\beta}_{\mu\nu}(\vec{r}_i)\end{aligned} \tag{6}$$

In eqs. 4–6 the index k runs over the N_{QM} QM nuclei, and Z_k and $\vec{R}_k$ denote the charge and position of the k-th nucleus, respectively. The electronic contributions are written in terms of the density matrix $P_{\mu\nu}$, where μ and ν label atomic orbitals, and the integrals $V_{\mu\nu}$, $\vec{E}_{\mu\nu}$ and $G^{\alpha\beta}_{\mu\nu}$ read:

$$V_{\mu\nu}(\vec{r}_i) = -\int_{\mathbb{R}^3} \frac{\chi_\mu(\vec{r})\chi_\nu(\vec{r})}{|\vec{r}_i - \vec{r}|}\mathrm{d}^3 r, \tag{7}$$

$$\vec{E}_{\mu\nu}(\vec{r}_i) = -\int_{\mathbb{R}^3} \frac{\chi_\mu(\vec{r})\chi_\nu(\vec{r})(\vec{r}_i - \vec{r})}{|\vec{r}_i - \vec{r}|^3}\,\mathrm{d}^3 r, \tag{8}$$

$$G^{\alpha\beta}_{\mu\nu}(\vec{r}_i) = -\int_{\mathbb{R}^3} \chi_\mu(\vec{r})\chi_\nu(\vec{r}) \left(\frac{3(r_i^\alpha - r^\alpha)(r_i^\beta - r^\beta)}{|\vec{r}_i - \vec{r}|^5} - \frac{\delta_{\alpha\beta}}{|\vec{r}_i - \vec{r}|^3}\right) \mathrm{d}^3 r. \tag{9}$$

Finally, the last term in eq. 2 is the variational polarization energy

$$\mathcal{E}^{\mathrm{Pol}}_{\mathrm{QM/MM}} = \frac{1}{2}\boldsymbol{\mu}_{\mathrm{d}}^\dagger \boldsymbol{T}\boldsymbol{\mu}_{\mathrm{p}} - \frac{1}{2}\Big(\boldsymbol{\mu}_{\mathrm{p}}^\dagger \boldsymbol{E}_{\mathrm{d}} + \boldsymbol{\mu}_{\mathrm{d}}^\dagger \boldsymbol{E}_{\mathrm{p}}\Big) + - \frac{1}{2}\big(\boldsymbol{\mu}_{\mathrm{p}} + \boldsymbol{\mu}_{\mathrm{d}}\big)^\dagger \mathbf{E}^{\mathrm{QM}}(\mathbf{P}). \tag{10}$$

This term accounts for the mutual polarization of the QM density and the AMOEBA induced dipoles. A more detailed derivation of the variational formulation of the AMOEBA polarization energy can be found in Ref. 20, while details on the AMOEBA induced dipoles $\boldsymbol{\mu}_{\mathrm{p}}$ and $\boldsymbol{\mu}_{\mathrm{d}}$, and the related electric fields are discussed in Ref. 39.

The use of a variational formalism makes the derivation of the coupled equations straightforward.The QM/AMOEBA Fock matrix is obtained as the gradient of the functional in 1 with respect to the density matrix:

$$\widetilde{\boldsymbol{F}} = \frac{\partial \mathcal{E}(\boldsymbol{P}, \boldsymbol{\mu})}{\partial \boldsymbol{P}} = \boldsymbol{F}^{\circ} + \boldsymbol{F}^{\mathrm{Env}}. \tag{11}$$

In eq. 11, $\boldsymbol{F}^{\circ}$ is the standard Fock matrix, while $\boldsymbol{F}^{\mathrm{Env}}$ is the contribution due to the embedding:

$$F^{\mathrm{Env}}_{\mu\nu} = \boldsymbol{q}^\dagger \boldsymbol{V}_{\mu\nu} - \boldsymbol{\mu}_{\mathrm{s}}^\dagger \boldsymbol{E}_{\mu\nu} - \boldsymbol{\Theta}^\dagger \boldsymbol{G}_{\mu\nu} - \frac{1}{2}(\boldsymbol{\mu}_{\mathrm{p}} + \boldsymbol{\mu}_{\mathrm{d}})^\dagger \boldsymbol{E}_{\mu\nu} \tag{12}$$

The Fock operator in eq. 11 can be used to set up a self-consistent field procedure. Since it depends on the AMOEBA induced dipoles, the AMOEBA polarization equations need to be solved at each SCF iteration. These are obtained by differentiating the energy functional in eq. 1 with respect to both sets of dipoles, and setting the derivative to zero, which yields:

$$\begin{aligned} \boldsymbol{T}\boldsymbol{\mu}_{\mathrm{p}} &= \boldsymbol{E}_{\mathrm{p}} + \boldsymbol{E}^{\mathrm{QM}}(\boldsymbol{P}) \\ \boldsymbol{T}\boldsymbol{\mu}_{\mathrm{d}} &= \boldsymbol{E}_{\mathrm{d}} + \boldsymbol{E}^{\mathrm{QM}}(\boldsymbol{P}). \end{aligned} \tag{13}$$

The two linear systems in eq. 13 can be easily solved by using an iterative method, as discussed in detail in refs. 40,41. In particular, in the present work we use Jacobi Iterations together with the direct inversion in the iterative subspace (DIIS) method[42] to accelerate convergence. To reduce the drift issue (see discussion in the Numerical section), all simulations are performed with a tight convergence threshold (10^{-8} D) for the dipoles.

2.1 Analytical derivatives of the QM/AMOEBA energy

We will now proceed with the derivation of the QM/AMOEBA gradients. We will focus the discussion on the QM/MM interaction energy, and in particular on the electrostatic and polarization terms, given in eqs. 3 and 10, respectively. Thanks to our variational formulation, we are only concerned with partial derivatives. By differentiating eq. 3 with respect to the coordinates of a QM nucleus k we get:

$$\frac{\partial \mathcal{E}^{\mathrm{El}}_{\mathrm{QM/MM}}}{\partial R_k^\alpha} = \mathbf{q}^\dagger \frac{\partial \mathbf{V}^{\mathrm{QM}}}{\partial R_k^\alpha} - \boldsymbol{\mu}_s^\dagger \frac{\partial \mathbf{E}^{\mathrm{QM}}}{\partial R_k^\alpha} - \boldsymbol{\Theta}^\dagger \frac{\partial \mathbf{G}^{\mathrm{QM}}}{\partial R_k^\alpha}. \tag{14}$$

Eq. 14 contains the derivatives of the potential, field and field gradient, as given in eqs. 4–6:

$$
\begin{aligned}
\frac{\partial V^{\mathrm{QM}}(\vec{r}_i;\boldsymbol{P})}{\partial R_k^\alpha} =& \frac{Z_k(r_i^\alpha - R_k^\alpha)}{|\vec{r}_i - \vec{R}_k|^3} + \sum_{\mu\nu}^{N_\mathrm{b}} P_{\mu\nu}\frac{\partial V_{\mu\nu}(\vec{r}_i)}{\partial R_k^\alpha} \\
\frac{\partial [E^{\mathrm{QM}}]^\beta(\vec{r}_i;\boldsymbol{P})}{\partial R_k^\alpha} =& Z_k\left(\frac{3(r_i^\alpha - R_k^\alpha)(r_i^\beta - R_k^\beta)}{|\vec{r}_i - \vec{R}_k|^5} - \frac{\delta_{\alpha\beta}}{|\vec{r}_i - \vec{R}_k|^3}\right) + \sum_{\mu\nu}^{N_\mathrm{b}} P_{\mu\nu}\frac{\partial E_{\mu\nu}^\beta(\vec{r}_i)}{\partial R_k^\alpha} \\
\frac{\partial [G^{\mathrm{QM}}]^{\beta\gamma}(\vec{r}_i;\boldsymbol{P})}{\partial R_k^\alpha} =& 3Z_k\frac{(r_i^\alpha - R_k^\alpha)\delta_{\beta\gamma} + (r_i^\beta - R_k^\beta)\delta_{\alpha\gamma} + (r_i^\gamma - R_k^\gamma)\delta_{\alpha\beta}}{|\vec{r}_i - \vec{R}_k|^5} \\
& - 15Z_k\frac{(r_i^\alpha - R_k^\alpha)(r_i^\beta - R_k^\beta)(r_i^\gamma - R_k^\gamma)}{|\vec{r}_i - \vec{R}_k|^7} + \sum_{\mu\nu}^{N_\mathrm{b}} P_{\mu\nu}\frac{\partial G_{\mu\nu}^{\beta\gamma}(\vec{r}_i)}{\partial R_k^\alpha},
\end{aligned} \tag{15}
$$

where the integral derivatives are defined as follows:

$$
\begin{aligned}
\frac{\partial V_{\mu\nu}(\vec{r}_i)}{\partial R_k^\alpha} =& -\int_{\mathbb{R}^3}\frac{\partial(\chi_\mu(\vec{r})\chi_\nu(\vec{r}))}{\partial R_k^\alpha}\frac{1}{|\vec{r}_i - \vec{r}|}\mathrm{d}^3r, \\
\frac{\partial E_{\mu\nu}^\beta(\vec{r}_i)}{\partial R_k^\alpha} =& -\int_{\mathbb{R}^3}\frac{\partial(\chi_\mu(\vec{r})\chi_\nu(\vec{r}))}{\partial R_k^\alpha}\frac{(r_i^\beta - r^\beta)}{|\vec{r}_i - \vec{r}|^3}\,\mathrm{d}^3r, \\
\frac{\partial G_{\mu\nu}^{\beta\gamma}(\vec{r}_i)}{\partial R_k^\alpha} =& -\int_{\mathbb{R}^3}\frac{\partial(\chi_\mu(\vec{r})\chi_\nu(\vec{r}))}{\partial R_k^\alpha} \\
& \left(\frac{3(r_i^\beta - r^\beta)(r_i^\gamma - r^\gamma)}{|\vec{r}_i - \vec{r}|^5} - \frac{\delta_{\beta\gamma}}{|\vec{r}_i - \vec{r}|^3}\right)\mathrm{d}^3r.
\end{aligned} \tag{16}
$$

Similarly, the gradient of the QM/AMOEBA polarization energy with respect to the position of a QM nucleus is:

$$
\frac{\partial \mathcal{E}_{\mathrm{QM/MM}}^{\mathrm{Pol}}}{\partial R_k^\alpha} = -\frac{1}{2}(\boldsymbol{\mu}_\mathrm{d} + \boldsymbol{\mu}_\mathrm{p})\frac{\partial \mathbf{E}^{\mathrm{QM}}(\mathbf{P})}{\partial R_k^\alpha}, \tag{17}
$$

with the derivative of the QM field given in eq. 15.

We now proceed to differentiate the QM/AMOEBA energy with respect to the positions of a MM atom. The electrostatic term gives rise to two different contributions. The first arises from the derivatives of the potential, field and field gradient, which are, respectively, the field, field gradient and field second derivative. The second contribution, which we will denote with $\vec{F}_{\mathrm{rot,i}}$, comes from the matrices that are used to rotate the static dipoles and quadrupoles from the molecular frame to the lab frame. The latter contribution is straightforward, but very cumbersome, and will not be discussed here. The reader can find a complete derivation in ref. 40. The derivative of the electrostatic energy with respect to the position of a classical atoms thus reads:

$$
\begin{aligned}
\frac{\partial \mathcal{E}_{\mathrm{QM/MM}}^{\mathrm{El}}}{\partial r_i^\alpha} =& \mathbf{q}^\dagger[\mathbf{E}^{\mathrm{QM}}]^\alpha - [\mathbf{G}^{\mathrm{QM}}]^{\alpha\beta}\boldsymbol{\mu}_s^\beta + \\
& -[\mathbf{O}^{\mathrm{QM}}]^{\alpha\beta\gamma}\boldsymbol{\Theta}^{\beta\gamma} + F_{\mathrm{rot,i}}^\alpha.
\end{aligned} \tag{18}
$$

where we introduced the second field derivative $\mathbf{O}^{\mathrm{QM}}$, whose components are given by:

$$[O^{\mathrm{QM}}]^{\alpha\beta\gamma}(\vec{r}_i;\boldsymbol{P}) = -\sum_k^{N_{QM}} Z_k \left(3\frac{(r_i^\alpha - R_k^\alpha)\delta_{\beta\gamma} + (r_i^\beta - R_k^\beta)\delta_{\alpha\gamma} + (r_i^\gamma - R_k^\gamma)\delta_{\alpha\beta}}{|\vec{r}_i - \vec{R}_k|^5} \right.$$
$$\left. - 15\frac{(r_i^\alpha - R_k^\alpha)(r_i^\beta - R_k^\beta)(r_i^\gamma - R_k^\gamma)}{|\vec{r}_i - \vec{R}_k|^7} \right) + \sum_{\mu\nu}^{N_{\mathrm{b}}} P_{\mu\nu} O_{\mu\nu}^{\alpha\beta\gamma}(\vec{r}_i), \tag{19}$$

and

$$O_{\mu\nu}^{\alpha\beta\gamma}(\vec{r}_i) = \int_{\mathbb{R}^3} \chi_\mu(\vec{r})\chi_\nu(\vec{r}) \left(3\frac{(r_i^\alpha - r^\alpha)\delta_{\beta\gamma} + (r_i^\beta - r^\beta)\delta_{\alpha\gamma} + (r_i^\gamma - r^\gamma)\delta_{\alpha\beta}}{|\vec{r}_i - \vec{r}|^5} \right.$$
$$\left. - 15\frac{(r_i^\alpha - r^\alpha)(r_i^\beta - r^\beta)(r_i^\gamma - r^\gamma)}{|\vec{r}_i - \vec{r}|^7} \right) \mathrm{d}^3 r. \tag{20}$$

The derivatives of the QM/AMOEBA polarization energy with respect to the position of an MM atom are given by:

$$\frac{\partial \mathcal{E}_{\mathrm{QM/MM}}^{\mathrm{Pol}}}{\partial r_i^\alpha} = \frac{1}{2}\boldsymbol{\mu}_d^\dagger \frac{\partial \boldsymbol{T}}{\partial r_i^\alpha}\boldsymbol{\mu}_p - \frac{1}{2}\Big(\boldsymbol{\mu}_{\mathrm{p}}^\dagger \frac{\partial \boldsymbol{E}_{\mathrm{d}}}{\partial r_i^\alpha} + \tag{21}$$
$$+\boldsymbol{\mu}_{\mathrm{d}}^\dagger \frac{\partial \boldsymbol{E}_{\mathrm{p}}}{\partial r_i^\alpha}\Big) - \frac{1}{2}[\mathbf{G}^{\mathrm{QM}}]^{\alpha\beta}(\boldsymbol{\mu}_d^\beta + \boldsymbol{\mu}_p^\beta).$$

The derivatives of the $\mathbf{T}$ matrix and of the $\boldsymbol{E}_{\mathrm{d}}$ and $\boldsymbol{E}_{\mathrm{p}}$ fields are again detailed in Ref. 40.

2.2 Acceleration the QM part through an Extended Lagrangian formalism

The so called Extended BO (XBO) Lagrangian, $\mathcal{L}^{\mathrm{XBO}}$, defined as in eq. 22, includes auxiliary EDFs, here expressed in terms of orthogonal electronic density matrices, $\mathbf{P}^*$ and its time derivative $\dot{\mathbf{P}}^*$, evolving on a harmonic potential centered at the SCF ground state solution $\mathbf{P}^{\mathrm{SCF}}$. In our implementation it is defined as the QM/AMOEBA SCF ground state potential $\mathcal{E}(\mathbf{R};\mathbf{P}^{SCF},\boldsymbol{\mu})$ for the real EDF. The third and fourth terms of the RHS of eq. 22 are the fictitious kinetic and potential energies of the auxiliary EDFs, relative to the fictitious electronic mass m and frequency ω.

$$\mathcal{L}^{\mathrm{XBO}}(\mathbf{R},\dot{\mathbf{R}},\mathbf{P}^*,\dot{\mathbf{P}}^*) = \frac{1}{2}\sum_I^{N_Z} M_I \dot{R}_I^2 - \mathcal{E}(\mathbf{R};\mathbf{P}^{\mathrm{SCF}},\boldsymbol{\mu}) + \frac{m}{2}\,\mathrm{Tr}[\dot{\mathbf{P}}^{*2}] - \frac{m\omega}{2}\,\mathrm{Tr}\left[(\mathbf{P}^{\mathrm{SCF}} - \mathbf{P}^*)^2\right] \tag{22}$$

In the limit $m \longrightarrow 0$, $\mathcal{L}^{\mathrm{XBO}} \longrightarrow \mathcal{L}^{\mathrm{BO}}$ and the evolution in time of the system is described by the Euler–Lagrange equations of motion

$$M_I \ddot{R}_I = -\frac{\partial \mathcal{E}(\mathbf{R};\mathbf{P}^{\mathrm{SCF}},\boldsymbol{\mu})}{\partial R_I} \tag{23}$$
$$\ddot{\mathbf{P}}^* = \omega^2(\mathbf{P}^{\mathrm{SCF}} - \mathbf{P}^*). \tag{24}$$

As shown in eq. 23, the nuclear degrees of freedom remain unaffected by the extended ones as in a regular BOMD.

The auxiliary EDFs are propagated in a Verlet scheme, as well as the nuclear coordinates, introducing a dissipative force term in a Langevin-like approach,[38] resulting in the following expression:

$$\mathbf{P}^*_{t_{n+1}} = 2\mathbf{P}^*_{t_n} - \mathbf{P}^*_{t_{n-1}} + k(\mathbf{P}_{t_n} - \mathbf{P}^*_{t_n}) + \quad (25)$$
$$+\alpha \sum_{l=0}^{K} c_l \mathbf{P}^*_{t_{n-l}}$$

where α is the coupling coefficient between the auxiliary EDFs and the external dissipative bath. Further details can be found in ref. 38 where also various optimized values for k, α and the linear combination parameters c_l are reported. This expression represents the improved density which will be used as a guess in the SCF procedure. Since the Gaussian code works with non-orthogonal density matrices, we propagate $\tilde{\mathbf{P}}^*_{t_n} = \mathbf{S}^{1/2}\mathbf{P}^*_{t_n}\mathbf{S}^{1/2}$ rather than $\mathbf{P}^*_{t_n}$, as proposed by Skylaris et al.[43] The initial guess is again given by eq. 25, after multiplying $\tilde{\mathbf{P}}^*_{t_{n+1}}$ by $\mathbf{S}^{-1/2}$ on left and right.

3 Numerical Tests

To perform hybrid polarizable QM/MM MD simulation, an interface between a locally modified version of Gaussian[25] and Tinker (and Tinker-HP) has been created. The work flow is described in details in Figure 1. In our implementation, Gaussian is used to solve the QM/MM equations and to compute the electrostatic and polarization QM/MM energy and forces. This allows us to minimize communication between Gaussian and Tinker, and to exploit our previous FMM-based linear scaling implementation of the polarizable electrostatics.[17] Tinker/Tinker-HP computes all MM non-electrostatic terms and, given the total forces, integrates the equations of motions. The QM/MM driver handles the communication between Gaussian and Tinker, and works directly on the input/output of each program.

As a test case we perform a series of QM/AMOEBA MD simulations of the alanine dipeptide (ADP) in a cubic box of 631 waters (1 912 atoms overall, see fig. 2). The dipeptide represents the QM subsystem in our hybrid approach and is treated at the B3LYP/6-31G level, while the water molecules are treated at the AMOEBA level.

We run several MD trajectories in the NVE ensemble, using a time step $\delta t = 0.5$ fs for a total simulation time of 1 ps. Here we discuss the tests we carried out to analyze the effect that the environment, the extrapolation scheme and the SCF convergence threshold have on the energy conservation. The SCF convergence thresholds tested are 10^{-3}, 10^{-5} and 10^{-8}. Note that convergence in Gaussian is based on the root mean square (RMS) variation of the electronic density, rather than the energy. The loosest value (10^{-3}) is chosen to mimic a strongly noised dynamics, with poorly converged density and inaccurate gradients. Since our simulations are run in the microcanonical ensemble, we cannot directly control temperature, except for the sampling of the initial velocities, obtained from a Maxwell–Boltzmann distribution.

The two extrapolation schemes employed are that of Niklasson *et al.*[37] (henceforth labeled TR–BOMD), and that of eq. 25 (XL–BOMD) with $K = 7$. While different values of K have been used in the literature,[43,44] we follow the work of Niklasson and coworkers,[45] where tight-binding DFT is applied to different amino acids and different K values are compared. Finally we test the effect of the environment by comparing the simulations in water with gas-phase simulations, keeping all the other settings unchanged.

We compare the drift in total energy and the noise in each of the twelve resulting trajectories. The drift is assumed to be linear in time, and is computed as the slope of the best line interpolating the time sequence of the energy values. The noise is evaluated as the root mean square of the energy fluctuations after removing the drift.[36] We also report the pseudo-temperature of the EDFs,[43,46] computed as $\mathrm{Tr}[\dot{\mathbf{X}}^2]/N_\mathrm{e}$, where $\mathbf{X} = \mathbf{P}^*$ or $\mathbf{P}^{SCF}$, the dot indicates time derivatives (performed

Figure 1: Work-flow diagram of the implementation and Gaussian/TINKER interface. The driver is a bash script overseeing the writing of input files and the exchange of informations between TINKER and Gaussian codes. TINKER is the main program as it collects the energy gradients computed by Gaussian and takes care of the nuclear classical dynamics. Gaussian solves the time-independent Schrödinger equation, computing the electronic PES on-the-fly and its derivative at each nuclear configuration.

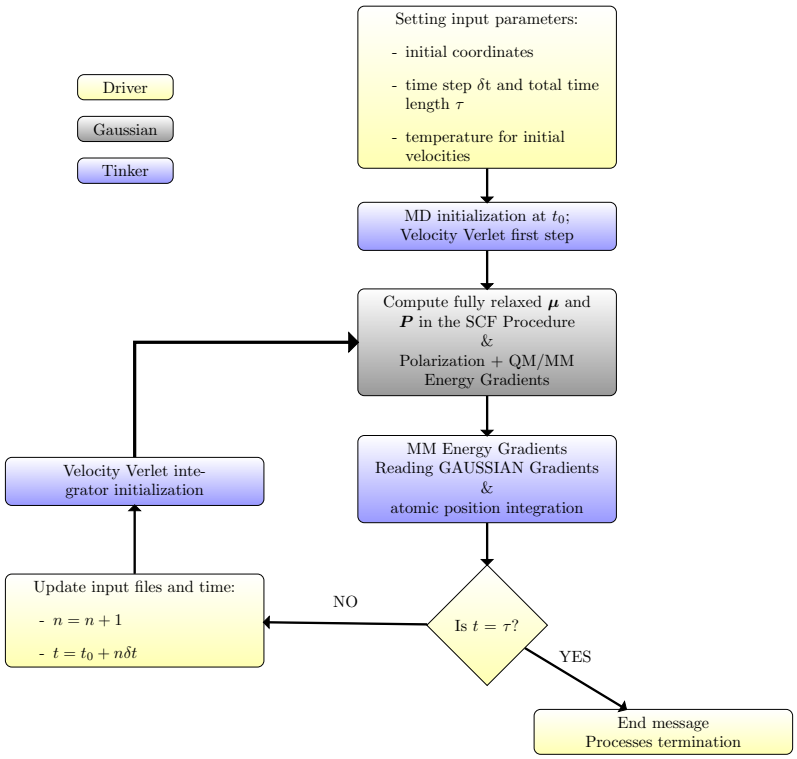

numerically), and N_e is the number of electrons. As starting geometry, we use a snapshot extracted from an Amber classical MD, and set a low temperature (50 K) for the initial velocity sampling. Since the temperature determines the amount of energy per vibrational degree of freedom, the energy oscillation amplitudes are temperature dependent. High-temperature simulations have the effect of increasing the noise, thus affecting the accuracy of our estimation of the energy drift, as shown in the Supporting Information where the results of a 300 K dynamics is reported (Figure S2).

The results are reported in Tab. 1. In Fig. 3, we plot the total energy as $E_{\text{tot}}(t) - E_{\text{avg}}$ for each simulation. Panels A and B refer to gas-phase and QM/AMOEBA simulations. The red lines represent the energy of TR–BO, using SCF convergence 10^{-3}. The insets clearly show that the energy diverges, reaching $\sim$2000 mE_H after 315 fs in gas-phase and 355 fs in water. Due to the high noise (92220 and 74810 μE_H respectively) and inaccuracy in the drift determination, the results are not meaningful and conclusion cannot be drawn on the dynamics conservativity.

Using the XL–BO extrapolation (Fig. 3, blue line, panels A, B), the results are more stable, as the energy does not diverge in either gas- and condensed- phase, although the drift is quite large ($\sim$ 2000 and $\sim$ 1000 μE_H/ps). Furthermore the average number of SCF cycles along the whole trajectory, $\overline{N}$, in XL–BO is almost half as that in TR–BO ($\sim$ 3 for XL–BO vs. $\sim$ 5 for TR–BO), as expected. Since the dissipative extended Lagrangian approach removes the numerical noise, the dynamics is more stable, even though the noise remains rather large ($\sim$ 3 and $\sim$ 4 mE_H in gas-phase and QM/AMOEBA, respectively).

The different behavior of the two approaches can be easily understood by plotting the pseudo-temperature of the auxiliary and real

Table 1: Comparison of the average number of SCF cycles ($\overline{N}$), total energy drift and noise between different convergence criteria, for both gas-phase and QM/AMOEBA BOMD, using eq. 7 in Ref. 37 (TR–BOMD) and eq. 25 (XL–BOMD) with $K = 7$ for the SCF guess extrapolation.
a: In this case the trajectory explodes around 315 fs in gas-phase and 355 fs in water, so the average number of SCF cycles, the drift and the noise are computed over these time intervals

Conv. (10^{-N})	Method	Gas-Phase $\overline{N}$	Gas-Phase Drift (μE_H/ps)	Gas-Phase noise (μE_H)	QM/AMOEBA $\overline{N}$	QM/AMOEBA Drift (μE_H/ps)	QM/AMOEBA noise (μE_H)
3	TR–BO[a]	5.4	72340 ± 79320	92220	5.1	54930 ± 53770	74810
	XL–BO	2.8	2090 ± 470	3190	2.7	1060 ± 530	3630
5	TR–BO	5.18	-9.0 ± 0.67	4.6	5.46	-82 ± 3.2	22
	XL–BO	3.62	-0.66 ± 0.74	5.0	3.78	-72 ± 3.2	22
8	TR–BO	7.29	-0.20 ± 0.19	1.3	7.40	-70 ± 3.2	22
	XL–BO	7.83	-0.21 ± 0.19	1.3	8.09	-70 ± 3.2	22

Figure 2: Snapshot extracted from an MD run. The ADP molecule in the center is the QM subsystem, surrounded by water molecules described with the AMOEBA polarizable FF.

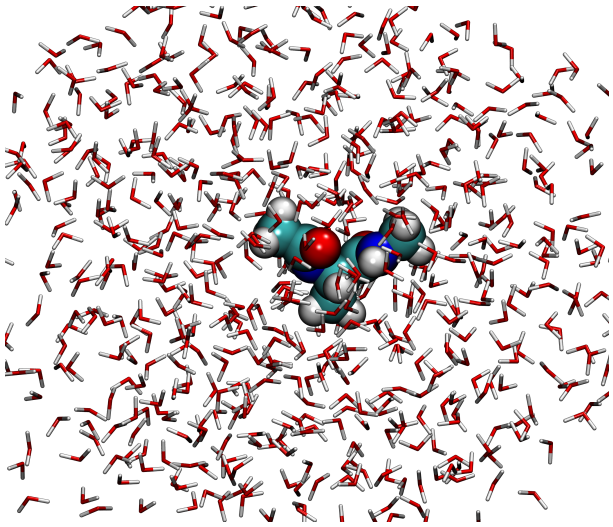

EDFs in the two cases. Fig. 4 shows the overheating of the auxiliary variables for TR–BO, which diverge significantly and quite rapidly (after ~ 200 fs) from the real converged density. This leads to a loss of computational efficiency, since the SCF procedure is no longer able to reach convergence. In the XL–BO case the two pseudo-temperatures remain quite close to each other.

Increasing the convergence threshold to 10^{-5} we obtain consistently better results, and we can observe a non-negligible differences between TR– and XL–BO (see Tab. 1, and Figure 3, panels C and D.). In gas-phase (red lines) both approaches give substantially no drift, even if XL–BO is still better, showing a smaller noise value and $\sim$ 30% less SCF cycles on average.

Comparing these results with the QM/AMOEBA ones (blue lines), we find that the drift and the noise are two and one orders of magnitude greater (XL–BO and TR–BO, respectively) than the corresponding values in gas-phase. This is due mainly to the effect of the MM polarization, since the iterative resolution for the induced dipoles causes the term $\frac{\partial E}{\partial \mu}$ to be not exactly zero, with a consequent non-zero Hellmann-Feynman residual forces. TR– and XL–BO schemes are almost equivalent in condensed phase, where the energy drift in our 1 ps test (panel D in Fig. 3) is noticeable although very small (10^{-1} mE_H).

The XL–BO still shows a 30% gain in SCF efficiency, which can be explained again with the EDFs pseudo-temperature analysis (see Supporting Information, Figure S1). We should also observe that, compared to a regular BOMD, the save in time is almost 50%.

Moving to the tightest convergence criterion (10^{-8}), almost no difference can be found comparing TR– and XL–BO within the same environment, and also no differences with XL–BO when the SCF convergence is set to 10^{-5}.

Figure 3: Energy variation (mE_H) along 1 ps-long trajectories. The plots on the left (A, C, E) refer to gas-phase simulations, those on the right (B, D, F) to simulations in water solution. Convergence thresholds are 10^{-3} (plots A and B), 10^{-5} (C and D), 10^{-8} (E and F). The insets in plots A, B and C show the full energy fluctuation range.

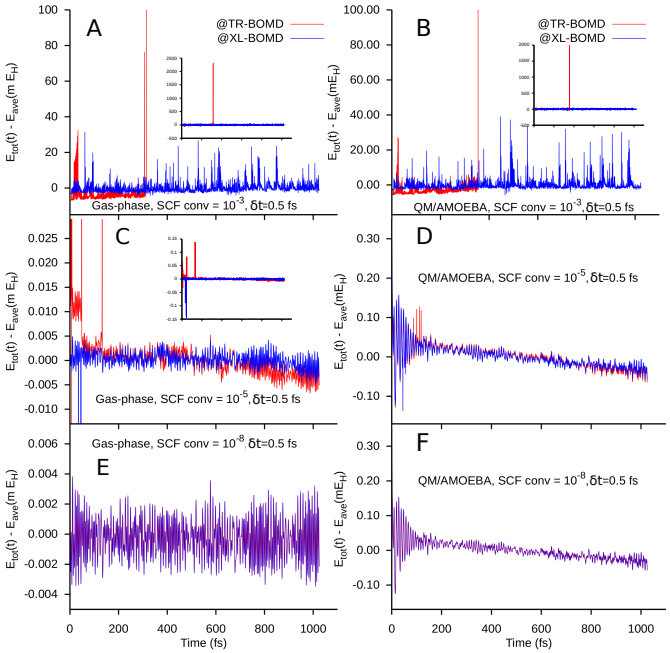

Figure 4: Comparison between the QM/AMOEBA auxiliary and real EDF pseudo-temperature for SCF convergence set to 10^{-3} in arbitrary units (a.u.). The values for the auxiliary EDFs are scaled by a factor 10^{-3} for TR–BO and 10^{-1} for XL–BO to obtain comparable scales

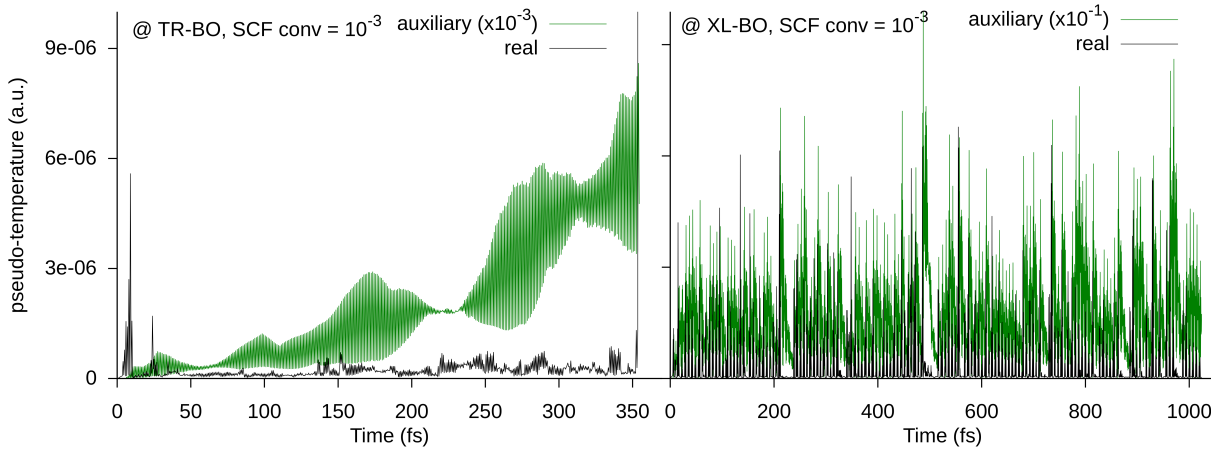

The same happens for the pseudo-temperature of the electronic variables, which we are not reporting.

We can then conclude that:

- for XL–BO, convergence for energy and energy gradients is reached already with a much lower convergence criterion than that usually suggested when QM forces have to be computed (10^{-8});
- as expected from theory, the perfectly lossless TR–BOMD is affected by the noise due to numerical approximation in the SCF solution. Nevertheless, as soon as well-converged densities are used, it is efficient in reducing the number of SCF cycles and produces a very stable simulation.

4 Conclusions

In this contribution, we presented an implementation of the analytical gradients of the polarizable QM/AMOEBA energy and of the machinery needed to perform efficient and stable molecular dynamics simulations. In particular, we used density functional theory as a quantum mechanical method, and the extended Born-Oppenheimer Lagrangian technique to provide an improved guess to the self-consistent field solver. Such a technique allows one to achieve energy-conserving and stable simulations, also offering remarkable computational advantages. We tested it by running several MD simulations on a small system, the alanine dipedptide (QM) solvated by water molecules (AMOEBA), comparing the TR– and XL–BO schemes using different SCF thresholds. We found that the XL–BO is the most effective approach when a moderately accurate convergence threshold is used, thanks to its capability to avoid the "heating" of the auxiliary EDFs, which remain close to the real ones along the dynamics. Our implementation is presently limited to systems where the MM portion is not covalently bonded to the QM one, and is therefore suited to study solute/solvent systems. A further implementation allowing to treat covalently bonded QM and MM systems is currently under investigation. This work represents a first step towards large scale polarizable QM/MM MD simulations and reactivity studies. More efficient and parallel computational strategies need to be used in order to extend the applicability of the method. In particular, in order to be able to treat large to very large systems, comprising up to tens of thousands of atoms in the classical subsystem, a scalable and efficient implementation of AMOEBA will be required, such as the one available in the Tinker HP suite of programs,[41,47,48] developed by some of us. Another aspect that needs to be addressed is the handling of boundary conditions. For non-periodic, polarizable QM/MM MD simulations, the use of a polarizable continuum as a boundary is particularly attractive.[49,50] Purely classical polarizable MD simulations within a polarizable continuum have already been discussed by some of us,[20] and are made possible by ddCOSMO, a fast, domain-decomposition-based implementation[51,52] of the conductor-like screening model.[53] An efficient and scalable implementation of a three-layer QM/AMOEBA/ddCOSMO model for molecular dynamics simulation is currently being investigated.

Acknowledgement This work was supported in part by French funds managed by CalSimLab and the ANR within the Investissements d Avenir program under reference ANR-11-IDEX-0004-02. J-PP and LL are grateful for support by the Direction Generale de l Armement (DGA) Maitrise NRBC of the French Ministry of Defense. The authors are indebted to Étienne Polack for providing the updated QM/MM driver. DL is grateful to Chris-Kriton Skylaris for helpful discussions on the extrapolation of the density matrix. JPP thanks Matt Challacombe and Christophe Raynaud for fruitful discussions

Supporting Information Available: Figure S1 and S2, reporting the pseudo-temperatures comparison between TR and XL–BO for SCF convergence 10^{-5} and 50 Vs 300 K dynamics respectively. This material is available free of charge via the Internet at `http://pubs.acs.org/`.

References

(1) Gresh, N.; Cisneros, G. A.; Darden, T. A.; Piquemal, J.-P. *J. Chem. Theory Comput.* **2007**, *3*, 1960–1986.

(2) Ponder, J. W.; Wu, C.; Ren, P.; Pande, V. S.; Chodera, J. D.; Schnieders, M. J.; Haque, I.; Mobley, D. L.; Lambrecht, D. S.; DiStasio, R. A.; Head-Gordon, M.; Clark, G. N. I.; Johnson, M. E.; Head-Gordon, T. *J.Phys. Chem. B* **2010**, *114*, 2549–2564.

(3) Bryce, R. A.; Buesnel, R.; Hillier, I. H.; Burton, N. A. *Chem. Phys. Lett.* **1997**, *279*, 367 – 371.

(4) Lipparini, F.; Barone, V. *J. Chem. Theory Comput.* **2011**, *7*, 3711–3724.

(5) Lipparini, F.; Cappelli, C.; Barone, V. *J. Chem. Theory Comput.* **2012**, *8*, 4153–4165.

(6) Lipparini, F.; Cappelli, C.; Barone, V. *J. Chem. Phys.* **2013**, *138*, 234108.

(7) Lamoureux, G.; MacKerell, A. D. J.; Roux, B. *J. Chem. Phys.* **2003**, *119*, 5185–5197.

(8) Boulanger, E.; Thiel, W. *J. Chem. Theory Comput.* **2012**, *8*, 4527–4538.

(9) Thompson, M. A.; Schenter, G. K. *J. Phys. Chem.* **1995**, *99*, 6374–6386.

(10) Jensen, L.; van Duijnen, P. T.; Snijders, J. G. *J. Chem. Phys.* **2003**, *119*, 3800.

(11) Nielsen, C. B.; Christiansen, O.; Mikkelsen, K. V.; Kongsted, J. *J. Chem. Phys.* **2007**, *126*, 154112.

(12) Illingworth, C. J. R.; Parkes, K. E. B.; Snell, C. R.; Ferenczy, G. G.; Reynolds, C. A. *J. Phys. Chem. A* **2008**, *112*, 12151–12156.

(13) Curutchet, C.; Muñoz-Losa, A.; Monti, S.; Kongsted, J.; Scholes, G. D.; Mennucci, B. *J. Chem. Theory Comput.* **2009**, *5*, 1838–1848.

(14) Si, D.; Li, H. *J. Chem. Phys.* **2010**, *133*, 144112.

(15) Steindal, A. H.; Ruud, K.; Frediani, L.; Aidas, K.; Kongsted, J. *J. Phys. Chem. B* **2011**, *115*, 3027–3037.

(16) Zeng, Q.; Liang, W. *J. Chem. Phys.* **2015**, *143*, 134104.

(17) Caprasecca, S.; Jurinovich, S.; Lagardère, L.; Stamm, B.; Lipparini, F. *J. Chem. Theory Comput.* **2015**, *11*, 694–704.

(18) Loco, D.; Polack, É.; Caprasecca, S.; Lagardère, L.; Lipparini, F.; Piquemal, J.-P.; Mennucci, B. *J. Chem. Theory Comput.* **2016**, *12*, 3654–3661.

(19) Lipparini, F.; Scalmani, G.; Mennucci, B.; Cancès, E.; Caricato, M.; Frisch, M. J. *J. Chem. Phys.* **2010**, *133*, 014106.

(20) Lipparini, F.; Lagardère, L.; Raynaud, C.; Stamm, B.; Cancès, E.; Mennucci, B.; Schnieders, M.; Ren, P.; Maday, Y.; Piquemal, J. P. *J. Chem. Theory Comput.* **2015**, *11*, 623–634.

(21) Kratz, E. G.; Walker, A. R.; Lagardère, L.; Lipparini, F.; Piquemal, J.-P.; Andrés Cisneros, G. *J. Comput. Chem.* **2016**, 1019–1029.

(22) Dziedzic, J.; Mao, Y.; Shao, Y.; Ponder, J.; Head-Gordon, T.; Head-Gordon, M.; Skylaris, C.-K. *J. Chem. Phys.* **2016**, *145*, 124106.

(23) Mao, Y.; Shao, Y.; Dziedzic, J.; Skylaris, C.-K.; Head-Gordon, T.; Head-Gordon, M. *J. Chem. Theory Comput.* **2017**, *13*, 1963–1979.

(24) Ponder, J. W. TINKER, Software Tools for Molecular Design. `http://dasher.wustl.edu/tinker`.

(25) Frisch, M. J. et al. Gaussian 09 Revision A.1. 2009; `www.gaussian.com`, Gaussian, Inc., Wallingford CT.

(26) Brunk, E.; Rothlisberger, U. *Chem. Rev.* **2015**, *115*, 6217–6263.

(27) Jensen, M. Ø.; Röthlisberger, U.; Rovira, C. *Biophys. J.* **2005**, *89*, 1744–1759.

(28) Alfonso-Prieto, M.; Biarns, X.; Vidossich, P.; Rovira, C. *J. Am. Chem. Soc.* **2009**, *131*, 11751–11761.

(29) Boero, M.; Ikeda, T.; Ito, E.; Terakura, K. *J. Am. Chem. Soc.* **2006**, *128*, 16798–16807.

(30) Marx, D.; Hutter, J. *Modern Methods and Algorithms of Quantum Chemistry*, 2nd ed.; John von Neumann Institute for Computing: Jülich, Germany, 2000.

(31) Car, R.; Parrinello, M. *Phys. Rev. Lett.* **1985**, *55*, 2471–2474.

(32) Payne, M. C.; Teter, M. P.; Allan, D. C.; Arias, T. A.; Joannopoulos, J. D. *Rev. Mod. Phys.* **1992**, *64*, 1045–1097.

(33) Tangney, P. *J. Chem. Phys.* **2006**, *124*, 044111.

(34) Millam, J.; Bakken, V.; Chen, W.; Hase, L.; Schlegel, H. B. *J. Chem. Phys.* **1999**, *111*, 3800–3805.

(35) Pulay, P.; Fogarasi, G. *Chem. Phys. Lett.* **2004**, *386*, 272–278.

(36) Herbert, J.; Head-Gordon, M. *Phys. Chem. Chem. Phys.* **2005**, *7*, 3269–3275.

(37) Niklasson, A. M. N.; Tymczak, C. J.; Challacombe, M. *Phys. Rev. Lett.* **2006**, *97*, 123001.

(38) Niklasson, A. M. N.; Steneteg, P.; Odell, A.; Bock, N.; Challacombe, M.; Tymczak, C. J.; Holmstrm, E.; Zheng, G.; Weber, V. *J. Chem. Phys.* **2009**, *130*, 214109.

(39) Ponder, J. W.; Wu, C.; Ren, P.; Pande, V. S.; Chodera, J. D.; Schnieders, M. J.; Haque, I.; Mobley, D. L.; Lambrecht, D. S.; DiStasio Jr, R. A.; Head-Gordon, M.; Clark, G. N. I.; Johnson, M. E.; Head-Gordon, T. *J. Phys. Chem. B* **2010**, *114*, 2549–2564.

(40) Lipparini, F.; Lagardre, L.; Stamm, B.; Cancs, E.; Schnieders, M.; Ren, P.; Maday, Y.; Piquemal, J.-P. *J. Chem. Theory Comput.* **2014**, *10*, 1638–1651.

(41) Lagardère, L.; Lipparini, F.; Polack, E.; Stamm, B.; Cancès, E.; Schnieders, M.; Ren, P.; Maday, Y.; Piquemal, J.-P. *J. Chem. Theory Comput.* **2015**, *11*, 2589–2599.

(42) Pulay, P. *Chem. Phys. Lett.* **1980**, *73*, 393–398.

(43) Vitale, V.; Dziedzic, J.; Albaugh, A.; Niklasson, A. M. N.; Head-Gordon, T.; Skylaris, C.-K. *J. Chem. Phys.* **2017**, *146*, 124115.

(44) Niklasson, A. M. N.; Steneteg, P.; Bock, N. *J. Chem. Phys.* **2011**, *135*, 164111.

(45) Zheng, G.; Niklasson, A. M. N.; Karplus, M. *J. Chem. Phys.* **2011**, *135*, 044122.

(46) Albaugh, A.; Demerdash, O.; Head-Gordon, T. *J. Chem. Phys.* **2015**, *143*, 174104.

(47) Narth, C.; Lagardère, L.; Polack, E.; Gresh, N.; Wang, Q.; Bell, D. R.; Rackers, J. A.; W., P. J.; Ren, P.; Piquemal, J.-P. *J. Comput. Chem.* **2016**, *37*, 494–505.

(48) Aviat, F.; Levitt, A.; Stamm, B.; Maday, Y.; Ren, P.; Ponder, J. W.; Lagardre, L.; Piquemal, J.-P. *J. Chem. Theory Comput.* **2017**, *13*, 180–190.

(49) Brancato, G.; Rega, N.; Barone, V. *J. Chem. Phys* **2006**, *124*, 214505.

(50) Brancato, G.; Nola, A. D.; Barone, V.; Amadei, A. *J. Chem. Phys* **2005**, *122*, 154109.

(51) Cancès, E.; Maday, Y.; Stamm, B. *J. Chem. Phys.* **2013**, *139*, 054111.

(52) Lipparini, F.; Stamm, B.; Cancès, E.; Maday, Y.; Mennucci, B. *J. Chem. Theory Comput.* **2013**, *9*, 3637–3648.

(53) Klamt, A.; Schuurmann, G. *J. Chem. Soc., Perkin Trans. 2* **1993**, 799–805.